Scaling law of Brownian rotation in dense hard-rod suspensions

Sheng Chen,[1] Wen Yan,[3] and Tong Gao[1,2,*]

[1]*Department of Mechanical Engineering, Michigan State University, East Lansing, Michigan 48864, USA*

[2]*Department of Computational Mathematics, Science and Engineering, Michigan State University, East Lansing, Michigan 48864, USA*

[3]*Center for Computational Biology, Flatiron Institute, Simons Foundation, New York, New York 10010, USA*

(Received 11 February 2020; revised 20 April 2020; accepted 2 July 2020; published 20 July 2020)

Self-diffusion in dense rod suspensions are subject to strong geometric constraints because of steric interactions. This topological effect is essentially anisotropic when rods are nematically aligned with their neighbors, raising considerable challenges in understanding and analyzing their impacts on the bulk physical properties. Via a classical Doi-Onsager kinetic model with the Maier-Saupe potential, we characterize the long-time rotational Brownian diffusivity for dense suspensions of hard rods of finite aspect ratios, based on quadratic orientation autocorrelation functions. Furthermore, we show that the computed nonmonotonic scalings of the diffusivity as a function of volume fraction can be accurately predicted by an alternative tube model in the nematic phase.

DOI: 10.1103/PhysRevE.102.012608

I. INTRODUCTION

Highly concentrated, or dense, suspensions of rodlike microparticles (e.g., polymers, macromolecules, and colloids) are abundant in both nature and the environment, where the rod motions are simultaneously subjected to the enhanced many-body interactions and thermal fluctuations [1–3]. Studying particle self-diffusion in these systems has a fundamental importance in understanding fluid and mass transport in biology, physics, chemical engineering, and material sciences and may suggest new control mechanisms such as particle self-assembly in microfluidic environments to form complex microstructures and patterns [4–6].

While prior studies have mostly focused on the dilute or semidilute cases, the diffusive properties of dense rod suspensions are poorly understood. Consider measuring the rotational diffusivity D_r for rods that undergo Brownian motions, which can be generally reconstructed from the relaxation history of the orientation autocorrelation function (OACF) [7]. In the semidilute regime, it approximately follows an exponential decay whose decay rate determines the unique value of D_r [2,3]. In the past decades, several mean-field-type models have been built to reveal the intrinsic scaling laws of D_r by virtually embedding a probe into the rod meshwork [2,8,9]. As an example, in the famous *tube* model proposed by Doi and Edwards (DE hereafter) [2], the probe is assumed to lie within an imaginary tube formed by neighbors. By estimating the probe's rotation angle before it disengages from the tube, the model predicts $D_r \sim (n\ell^3)^{-2}$, where n is the number density and ℓ the rod length. These semidilute models have been verified in both experiments and particle simulation studies, and have been widely used in characterizing Brownian rotations in polymers and liquid crystals [10–15].

When the volume fraction further increases, more and more frequent rod-rod collisions can drive isotropic-anisotropic (nematic, smectic, etc.) order transitions for densely packed rods [1,2]. Intriguingly, experiments have revealed that the OACFs may exhibit multiscale and shape-dependent behaviors for rods with different aspect ratios as the phase transition occurs [16–18], which raise considerable challenges in characterizing D_r. On the one hand, it is difficult to resolve the fast-growing complexity of many-body interactions using the theories of cluster-expansion type [19,20] when the expansion goes beyond the pairwise-level in virial expansion of free energy. On the other hand, the mean-field models like DE's are not applicable in the ordered phases (nematic or smectic) when the rods are subjected to strong anisotropic steric confinements. Hence there is a general lack of theoretical models for dense rod suspensions that are able to (1) precisely extract D_r from the measured OACF data and (2) interpret their analytical properties.

In this article we characterize the long-time Brownian rotational diffusivity D_r for dense rod suspensions via a Doi-Onsager model where a Maier-Saupe (MS) potential is employed to capture the isotropic-nematic (I-N) phase transition. When the hydrodynamic interactions are neglected, we show that the measured nonmonotonic D_r over a wide range of aspect ratios can be explained by a modified DE's tube model. By using a geometric constrained Brownian dynamics (GCBD) algorithm [21], we build our theory based on extensive numerical simulation data of N Brownian spherocylinders, each with length ℓ, diameter b, and orientation $\mathbf{p}$, in a cubic domain of length L. This method verified the classic Brownian spherocylinders without hydrodynamic interactions investigated by Bolhuis *et al.* [22] (see Ref. [21] for more details). Our simulations cover a wide range of aspect ratio $\gamma = \ell/b$ and extend to volume fraction $\phi = \pi n(\frac{b^3}{6} + \frac{\ell b^2}{4})$ over 50% (i.e., close to the nematic-smectic phase transition [22]), where $n = N/L^3$ is the particle number density. As shown by the open squares in Fig. 1, we perform an ensemble average and calculate the (global) orientational order parameter $S = \frac{3}{2N}\sum_{i=1}^{N}(\mathbf{p}_i \cdot \hat{\mathbf{n}})^2 - \frac{1}{2}$ and $\hat{\mathbf{n}}$ the average orientation of spherocylinders (i.e., the director [1,2]), which

*gaotong@egr.msu.edu

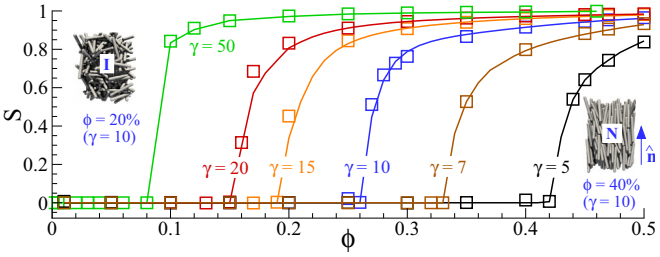

FIG. 1. Equilibrium orientational order parameter S as a function of ϕ. The open squares represent the GCBD simulation data. The solid lines are calculated using $\Psi_{\rm eq}$ in Eq. (2). Inset: Instantaneous snapshots at $\phi = 20\%$ and 40% for $\gamma = 10$ correspond to the I and N phase, respectively.

captures the first-order I-N transition as bifurcations of $S(\phi)$ curves.

II. KINETIC MODEL FOR D_r

A classical Doi-Onsager kinetic model [2] accurately describes the above mentioned critical behaviors via a time evolution equation

$$\frac{\partial \Psi}{\partial t} = D_r \mathcal{R} \cdot \left[\mathcal{R}\Psi + \frac{\Psi}{k_B T} \mathcal{R} U_s(\mathbf{p}) \right], \tag{1}$$

where Ψ is a probability distribution function (PDF) for a rod's orientation (unit) vector $\mathbf{p}$, and $\mathcal{R} = \mathbf{p} \times (\partial/\partial \mathbf{p})$ is a rotational operator. In the above, D_r characterizes the long-time Brownian rotational diffusion for an equilibrium rod system [2,15]. A mean-field torque is imposed on the rod's rotational dynamics via the MS potential [23–25] $U_s(\mathbf{p}) = -\zeta_0 \mathbf{pp}{:}\mathbf{Q}$ due to the crowdedness nature of densely packed rods, where $\mathbf{Q} = \langle \mathbf{pp} - \mathbf{I}/3 \rangle$ is the nematic-order-parameter tensor with $\langle\,\rangle$ a configurational average of $\mathbf{p}$, and ζ_0 is a strength coefficient. At equilibrium (i.e., $\frac{\partial \Psi}{\partial t} = 0$), we rewrite the MS potential as $U_s^{(\rm eq)} = -\zeta_0 \mathbf{pp}{:}\mathbf{Q}_{\rm eq}$ with $\mathbf{Q}_{\rm eq} = S(\hat{\mathbf{n}}\hat{\mathbf{n}} - \mathbf{I}/3)$, and then balance the rotational diffusion and the steric torque to obtain the equilibrium PDF,

$$\Psi_{\rm eq}(\theta) = \frac{\exp\left(\frac{S\zeta_0}{2k_B T} \cos 2\theta\right)}{2\pi \int_0^\pi \exp\left(\frac{S\zeta_0}{2k_B T} \cos 2\theta'\right) \sin\theta' \, d\theta'}, \tag{2}$$

with $\theta = \arccos(\mathbf{p} \cdot \hat{\mathbf{n}})$ [24,26]. As shown by the solid lines in Fig. 1, the equilibrium PDF can be fixed by calibrating the coefficient ζ_0 using the order parameter S measured in the GCBD simulations (see details in Appendix A).

We examine the orientation relaxation process of a free probe in an equilibrium particle bath. As examples of $\gamma = 20$ shown in Fig. 2(a), direct measurements of long-time $\langle \mathbf{p}(t) \cdot \mathbf{p}(0) \rangle$ often show overly complicated evolution behaviors as the system deviates from the isotropic cases (e.g., $\phi = 10\%$) whose OACFs decay exponentially to zero [2]. In the weak nematic (W-N) regimes (e.g., $\phi = 17\%$), however, the functions may exhibit extraordinary slow decays after the initial transient [27], which is different from the quick decays observed in the strong nematic (S-N) regime (e.g., $\phi = 40\%$). As an alternative approach shown in Fig. 2(b), when measuring the quadratic form $\langle [\mathbf{p}(t) \cdot \mathbf{p}(0)]^2 \rangle$ (or equivalently $\langle P_2[\mathbf{p}(t) \cdot \mathbf{p}(0)] \rangle$, P_2 represents the Legendre polynomial of

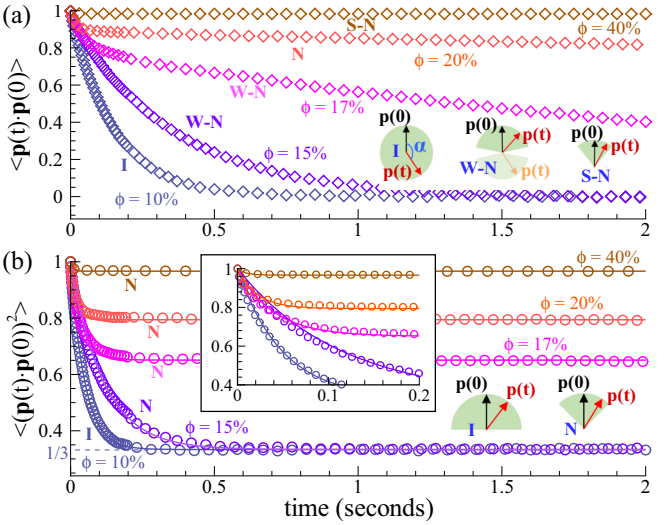

FIG. 2. Orientation relaxation characterized by $\langle \mathbf{p}(t) \cdot \mathbf{p}(0) \rangle$ (a) and $\langle [\mathbf{p}(t) \cdot \mathbf{p}(0)]^2 \rangle$ (b) across ϕ for $\gamma = 20$. The open symbols represent the GCBD data. Schematics of configurational space of $\mathbf{p}(t)$ are highlighted at the bottom for the different phases. In panel (b), the solid lines represent the fitting function in Eq. (3). Inset: Zoom-in window highlights that the short-time relaxation of OACF fits an exponential decay governed by a single timescale τ_R.

order 2 [2,14,28]); we observe that for all cases, the OACFs approach constant values after the initial decay, which can be fitted into a universal form

$$[\mathbf{p}(t) \cdot \mathbf{p}(0)]^2 \rangle = (1 - A_\infty) \exp\left(-\frac{t}{\tau_R}\right) + A_\infty \tag{3}$$

with the steady-state value of A_∞ and the correlation time τ_R that dominates the decay. In the isotropic regime ($\phi < 15\%$), $A_\infty = 1/3$, which has been proven analytically [2].

These behaviors can be qualitatively understood by examining the long-time orientation distribution of $\mathbf{p}(t)$ with respect to $\mathbf{p}(0)$. As sketched in the bottom of Fig. 2(a), the configurational space of $\mathbf{p}(t)$ exhibits spherical symmetry with the formed angle $\alpha = \arccos[\mathbf{p}(t) \cdot \mathbf{p}(0)] \in [0, \pi]$. In the S-N regime, it approximately reduces to a small and narrow cone-shaped domain with an acute angle α when the probe rotation is strongly confined around $\mathbf{p}(0)$. The cone shape can be described by its maximum opening angle estimated as $\alpha_{\rm max} \sim \pi/2 - \arcsin(S)$. In the W-N regime where rods are weakly aligned, $\mathbf{p}(t)$ can simultaneously fall into two large cones that are symmetric about $\alpha = \pi/2$ but with unequal probabilities as marked by different colors for the cones. A biased distribution of $\mathbf{p}(t)$ towards $\alpha = 0$ will cause a slower relaxation process (e.g., $\phi = 17\%$) towards a finite equilibrium value as $t \to \infty$. On the other hand, as shown in Fig. 2(b), a quadratic OACF maintains the fore-aft symmetry, i.e., $\langle [\mathbf{p}(t) \cdot \mathbf{p}(0)]^2 \rangle = \langle [-\mathbf{p}(t) \cdot \mathbf{p}(0)]^2 \rangle$. Hence the configurational domain of $\mathbf{p}(t)$ automatically switches from a half sphere in the isotropic regime to a single cone domain in the nematic regime, leading to all positive correlations at equilibrium (i.e., $A_\infty > 0$).

Next, we construct a mathematical model to connect the quadratic OACF with the Brownian diffusivity D_r defined in Eq. (1). We follow DE's theory [2,28] to define

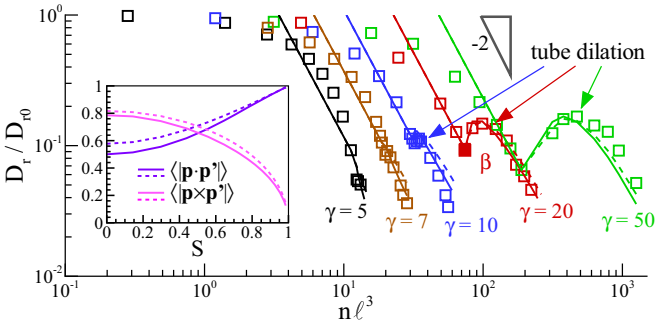

FIG. 3. D_r/D_{r0} as functions of $n\ell^3$ across ϕ for various γ. The open squares represent the data extracted from GCBD simulations via Eq. (6). The solid and dashed lines represent the scaling laws in Eqs. (10) and (12), respectively. The solid red square on the $\gamma = 20$ curve marks the location of the data for fitting β. Inset: $\langle|\mathbf{p}\times\mathbf{p}'|\rangle^{p}_{p'}$ and $\langle|\mathbf{p}\cdot\mathbf{p}'|\rangle^{p}_{p'}$ as functions of S, evaluated using $\Psi_{\rm eq}$ (solid lines) and the quadratic-closure approximation (dashed lines), respectively.

$\langle[\mathbf{p}(t)\cdot\mathbf{p}(0)]^2\rangle = \int(\mathbf{pp}{:}\mathbf{p}'\mathbf{p}')G(\mathbf{p},\mathbf{p}';t)\Psi_{\rm eq}(\mathbf{p}')d\mathbf{p}\,d\mathbf{p}'$ where a Green's function $G(\mathbf{p},\mathbf{p}';t)$ represents a conditional (or joint) probability that the probe is in the direction $\mathbf{p}$ at time t, given that it was in the direction $\mathbf{p}(0)$ at $t=0$. Starting from Eq. (1) with $U_s = U_s^{(\rm eq)}$, we can derive the evolution over time (see Appendix B)

$$\frac{\partial}{\partial t}\langle[\mathbf{p}(t)\cdot\mathbf{p}(0)]^2\rangle = -6D_r\left\{(1+q)\langle[\mathbf{p}(t)\cdot\mathbf{p}(0)]^2\rangle - \left(q+\frac{1}{3}\right)\right\}, \quad (4)$$

where $q(S) = \frac{2\zeta_0}{9k_BT}S(S+\frac{1}{2})$ captures the intrinsic I-N transition and admits the time-dependent solution

$$[\mathbf{p}(t)\cdot\mathbf{p}(0)]^2\rangle = \frac{2\exp[-6(1+q)D_rt]+3q+1}{3(1+q)}. \quad (5)$$

Therefore, comparing Eq. (3) and (5) yields $A_\infty = \frac{3q+1}{3(1+q)}$ and

$$D_r = \frac{1-A_\infty}{4\tau_R}, \quad (6)$$

which enable us to extract D_r from OACF data. It recovers the classical results $A_\infty = 1/3$ in the isotropic regime when $q=0$ [2,14]. For all cases, we present the ratio D_r/D_{r0} (D_{r0} is the diffusivity of an isolated rod) as functions of a dimensionless number density $n\ell^3$ in Fig. 3. After the I-N transition, D_r/D_{r0} for short rods (e.g., $\gamma = 5$) switches to an even faster decay, suggesting stronger hindrance on diffusion in the nematic phase. In contrast, reverse growths are seen for long rods (e.g., $\gamma > 10$) right after the I-N transition; while in the deep nematic regime, D_r/D_{r0} becomes descending again as the diffusive motions are fully constrained. All these results qualitatively agree with the experimental observations for rodlike molecules with different aspect ratios [16–18,29–31].

III. TUBE MODEL

To understand the complex scaling laws of D_r, as sketched in Fig. 4(a), we envision the rotation of a probe to be

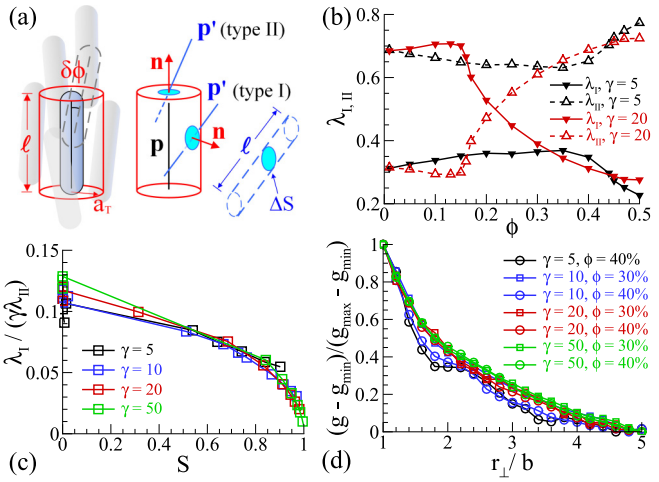

FIG. 4. GCBD simulations motivate a new tube model. (a) Schematic of a virtual tube with penetrations from both the sidewall and the two ends. (b) Fractional contributions of the averaged collision numbers on the sidewall (λ_I) and the ends (λ_{II}) for $\gamma = 5$ and 20 as functions of ϕ. (c) The collision number ratio $\lambda_I/(\gamma\lambda_{II})$ as functions of S for various γ. (d) The OPCF $g(r_\perp)$ in the nematic regime as functions of the dimensionless transverse distance $r_\perp/b$.

confined by surrounding neighbors that are nematically aligned. Inspired by DE's classical theory [2], we enclose the probe in a virtual tube. Unlike DE's original semidilute model which considers only one effective side-by-side interaction between an infinitesimally thin probe and its nearest neighbor, we simultaneously track multiple interactions (contacts) attributed from two types of collisions: side-side collisions (denoted by "type I") and end-side or end-end collisions (denoted by "type II"). Intuitively, type II collisions, which were neglected in DE's model, may significantly change the rotational motion because the collision forces have longer moment arms when it occurs at the probe's end.

The conceptual image in Fig. 4(a) of a restricted collision-driven rotational motion is supported by a series of GCBD simulation data that reveal intriguing geometric features. As shown in Fig. 4(b), we examine the fractional contributions of the two types of collisions relative to the total number of collisions, i.e., $\lambda_{I,II} = N_{I,II}/(N_I+N_{II})$, where $N_{I,II}$ represent the time-average collision numbers. For short rods (e.g., $\gamma = 5$), the type II collisions dominate in both the isotropic and nematic regimes; while for relatively long rods (e.g., $\gamma = 20$), the type I collisions are more frequent in the isotropic regime, but they are significantly reduced after the I-N transition and become much less compared to the type II collisions in the nematic regime. Not surprisingly, all data for a rescaled collision number ratio $\lambda_I/(\gamma\lambda_{II})$ approximately collapse onto a master curve since the collision numbers are purely determined by the surface areas of the sidewall and the ends. In Fig. 4(d) we define an orientational pair-correlation function (OPCF) in the rod's transverse direction [32–34]

$$g(r_\perp) = \frac{\sum_{i\neq j}\langle P_2(\mathbf{p}_i\cdot\mathbf{p}_j)\delta[r_\perp - \sqrt{|\mathbf{r}_{ij}|^2-(\mathbf{r}_{ij}\cdot\mathbf{p}_i)^2}]\rangle}{\sum_{i\neq j}\langle\delta[r_\perp - \sqrt{|\mathbf{r}_{ij}|^2-(\mathbf{r}_{ij}\cdot\mathbf{p}_i)^2}]\rangle}, \quad (7)$$

where $\mathbf{r}_{ij}$ connects the center-of-mass positions of the ith and jth rods, and $r_\perp$ measured the projected distance between the rods in perpendicular direction of $\mathbf{p}_i$. Again, all data for a rescaled OPCF $\frac{g(r_\perp)-g_{\min}}{g_{\max}-g_{\min}}$ by using the maximum (when $r_\perp = b$) and minimum (when $r_\perp > 4b$) values of g, especially for rods of high aspect ratios, approximately fall onto a master curve. These shape-independent features provides guidance of how to construct analytical models that accurately reflect the relative contributions of two types of steric interactions.

As illustrated in Fig. 4(a), we assume a probe oriented in the $\mathbf{p}$ direction has a thickness b and length ℓ, sitting among nematically aligned neighbors whose orientation distribution can be described by $\Psi_{\rm eq}$. We estimate the number of penetrations into a virtual tube that has the same rod length ℓ. As suggested by Fig. 4(d), the tube radius a_T approximately varies between b and $3b$ where the OPCFs exhibit significant correlations. Following DE's approach [2], we consider the number of rods that penetrate a small surface area ΔS with a unit normal vector $\mathbf{n}$ that can be calculated as $\Delta\mathcal{N} = n\ell\Delta S\langle|\mathbf{p}'\cdot\mathbf{n}|\rangle$ where the configurational average is performed in a representative volume along the $\mathbf{p}'$ direction. For the sidewall intersections (i.e., $\mathbf{n}\perp\mathbf{p}$) arising from the type I collisions, we reuse DE's calculation [2] to sum $\Delta\mathcal{N}$ over half of the sidewall area $S_I = \pi a_T\ell$ by taking into account the double penetration from a vicinal rod, and obtain the number $\mathcal{N}_I = S_I n\ell\langle|\mathbf{p}\cdot\mathbf{n}|\rangle^p_{p'} = 2na_T\ell^2\langle|\mathbf{p}\times\mathbf{p}'|\rangle^p_{p'}$ (see the derivation details in Ref. [2]). Here $\langle\,\rangle^p_{p'}$ represents configurational averages over both $\mathbf{p}$ and $\mathbf{p}'$. Likewise, the number of rods intersecting from the two ends (i.e., $\mathbf{n}/\!/\mathbf{p}$ and the total area $S_{II} = 2\pi a_T^2$) can be calculated in a straightforward manner as $\mathcal{N}_{II} = S_{II}n\ell\langle|\mathbf{p}\cdot\mathbf{n}|\rangle^p_{p'} = 2n\pi a_T^2\ell\langle|\mathbf{p}\cdot\mathbf{p}'|\rangle^p_{p'}$ by assuming that the surrounding rods penetrate the tube only once.

To avoid double counting the neighboring rods that penetrate from the side and one end simultaneously, we calculate the total penetration number as

$$\begin{aligned}\mathcal{N}_p &= \omega_I\mathcal{N}_I + \omega_{II}\mathcal{N}_{II}\\ &= 2\omega_I na_T\ell^2\langle|\mathbf{p}\times\mathbf{p}'|\rangle^p_{p'} + 2\omega_{II}n\pi a_T^2\ell\langle|\mathbf{p}\cdot\mathbf{p}'|\rangle^p_{p'}.\end{aligned}\tag{8}$$

Since the calculations of $\mathcal{N}_{I,II}$ have incorporated the shape effect, according to Fig. 4(c), we assume the weights $\omega_{I,II}(S)$ are shape-independent and will be selected such that $\mathcal{N}_I$ and $\mathcal{N}_{II}$ coexist in the isotropic regime but $\mathcal{N}_I$ vanishes in the "sharply aligned" limit where all rods are perfectly aligned (i.e., $S = 1$). We assume the probe rotates a small angle $\delta\phi$ as it moves for a distance of rod length ℓ during the "reptation" timescale $\tau_0 \propto D_{r0}^{-1}$, which leads to $D_r = \delta\phi^2/\tau_0 = \beta\delta\phi^2 D_{r0}$ with β a shape-dependent constant. Considering the fact that the probe encounters these $\mathcal{N}_p$ penetrations with equal probability, we estimate $\delta\phi = \frac{a_T}{\mathcal{N}_p\ell}$, yielding

$$\frac{D_r}{D_{r0}} = \beta(n\ell^3)^{-2}\left[\omega_I\langle|\mathbf{p}\times\mathbf{p}'|\rangle^p_{p'} + \pi\omega_{II}\left(\frac{a_T}{\ell}\right)\langle|\mathbf{p}\cdot\mathbf{p}'|\rangle^p_{p'}\right]^{-2}.\tag{9}$$

The β value for each γ case can be numerically fitted by matching D_r/D_{r0} with the GCBD data on a point where the I-N transition occurs (as one example, see the solid red square marked on the $\gamma = 20$ curve in Fig. 3) [2,11,12,35,36].

After β is fixed, we find that choosing $\omega_I = \langle|\mathbf{p}\times\mathbf{p}'|\rangle^p_{p'}$, $\omega_{II} = \langle|\mathbf{p}\cdot\mathbf{p}'|\rangle^p_{p'}$, and the tube radius $a_T \approx 2b$ leads to analytical results (lines) that are in excellent agreement with the GCBD data (symbols) as shown in Fig. 3. The analytical form can be written as

$$\frac{D_r}{D_{r0}} = \beta(n\ell^3)^{-2}\left[\left(\langle|\mathbf{p}\times\mathbf{p}'|^p_{p'}\right)^2 + \frac{2\pi}{\gamma}\left(\langle|\mathbf{p}\cdot\mathbf{p}'\rangle^p_{p'}\right)^2\right]^{-2},\tag{10}$$

where the two double-configurational averages are evaluated by using $\Psi_{\rm eq}$. The inset of Fig. 3 reveals the intrinsic competing mechanism for the nonmonotonic critical behaviors of D_r. Mathematically, we see that the enhanced rotational diffusions observed in the nematic phase are caused by the divergent behaviors of Eq. (10) as $\langle|\mathbf{p}\times\mathbf{p}'|\rangle^p_{p'}$ approaches zero at large S, which suggests weakened side-side steric interactions as the probe reptates. Such "tube dilation" effect is regulated by the enhanced end-steric effects in the nematic regime as $\langle|\mathbf{p}\cdot\mathbf{p}'|\rangle^p_{p'}$ dominates, especially for relatively short rods with small γ. Furthermore, we adopt a quadratic closure (see Appendix C) to approximate

$$\langle|\mathbf{p}\times\mathbf{p}'|\rangle^p_{p'} \approx \sqrt{\frac{2}{3}(1-S^2)}, \quad \langle|\mathbf{p}\cdot\mathbf{p}'|\rangle^p_{p'} \approx \sqrt{\frac{1}{3}(1+2S^2)}.\tag{11}$$

Then Eq. (10) can be rewritten as

$$\frac{D_r}{D_{r0}} \approx \beta(n\ell^3)^{-2}\left[\left(1+\frac{\pi}{\gamma}\right) + \left(\frac{2\pi}{\gamma}-1\right)S^2\right]^{-2}.\tag{12}$$

As shown by the dashed lines in Fig. 3, the above equation provides an accurate yet convenient form without using $\Psi_{\rm eq}$. For thin rods ($\gamma \to \infty$), Eq. (12) captures the DE's semidilute theory in the isotropic regime when $S = 0$. It also recovers DE's correction in the nematic regime when $S > 0$ and $\gamma \to \infty$ by considering the tube-dilation effect only [2,37,38], which, however, becomes singular in the limit $S \to 1$. We can further predict that such dilation effects occur only for rods with $\gamma > 2\pi$ as the resultant negative sign of the S^2 term directly causes reverse growing. This can be verified by the $\gamma = 7$ case where D_r/D_{r0} approximately follows the $(n\ell^3)^{-2}$ law in the nematic regime.

IV. CONCLUSION

In summary, we have built a Doi-Onsager model for characterizing the long-time Brownian diffusivity D_r in the nematic regime for concentrated rod suspensions. The nonmonotonic critical behaviors of D_r are accurately captured via an alternative tube model. We have shown that when appropriately incorporating steric hindrances around a probe rod, DE's tube concept can elegantly yet accurately describe topologically constrained rod rotation in a concentrated meshwork without scrutinizing detailed rod-rod interactions. While hydrodynamic interactions are neglected, we expect our scaling law remains accurate for dense rod suspensions where the short-range steric shielding dominates. We anticipate this model will provide an alternative angle in characterizing Brownian rotations in a wide variety of computational and experimental studies of soft condensed matter.

ACKNOWLEDGMENTS

T.G. and S.C. acknowledge the National Science Foundation Grants No. 1619960 and No. 1943759, and the computation resources from the Flatiron Institute and MSU's High Performance Computing Center.

APPENDIX A: EQUILIBRIUM PDF SOLUTION

The rod system can be described by a probability distribution function $\Psi(\mathbf{p})$ as a function of the orientation vector $\mathbf{p}$, evolved through the Smoluchowski equation (1). The equilibrium solution satisfies

$$\nabla_p \ln \Psi_{\rm eq} = \frac{2\zeta_0}{k_B T}(\mathbf{I} - \mathbf{pp}) \cdot \mathbf{Q} \cdot \mathbf{p}. \tag{A1}$$

In an isotropic state, $\Psi = \frac{1}{4\pi}$ with the coefficient $\zeta_0 = 0$. In the nematic regime, we assume the rods are distributed axisymmetrically around the director $\hat{\mathbf{n}}$, yielding [24,25]

$$\mathbf{Q} = S\left(\hat{\mathbf{n}}\hat{\mathbf{n}} - \frac{\mathbf{I}}{3}\right), \tag{A2}$$

where the order parameter S can be expressed as

$$S = \frac{1}{2}\int_0^{2\pi}\int_0^{\pi} \Psi(3\cos^2\theta - 1)\sin\theta\, d\theta\, d\phi. \tag{A3}$$

By substituting (A2) and (A3) into (A1), we can solve $\Psi(\theta)$ in spherical coordinates as

$$\Psi_{\rm eq}(\theta) = \frac{\exp\left[\chi\cos(2\theta)\right]}{2\pi\int_0^{\pi}\exp\left[\chi\cos(2\theta')\right]\sin\theta'\, d\theta'}, \tag{A4}$$

with the coefficient $\chi = \frac{S\zeta_0}{2k_BT}$. For a given ϕ and γ, χ can be measured through the following steps: (1) take log on both sides of (A4), yielding $\log\Psi_{\rm eq} = \chi\cos(2\theta) + \text{const}$; (2) construct a discrete orientation probability distribution from particle simulation by dividing θ uniformly into small intervals $\triangle\theta = \pi/400$; and (3) take log on the discrete orientation probability distribution and convert it to be a function of $\cos(2\theta)$ and use the linear fitting to get χ. After χ is measured, a continuous PDF can be constructed based on (A4). As examples shown in Fig. 5 for $\gamma = 10$ cases, the reconstructed PDF $\Psi_{\rm eq}$ accurately represent the numerical data.

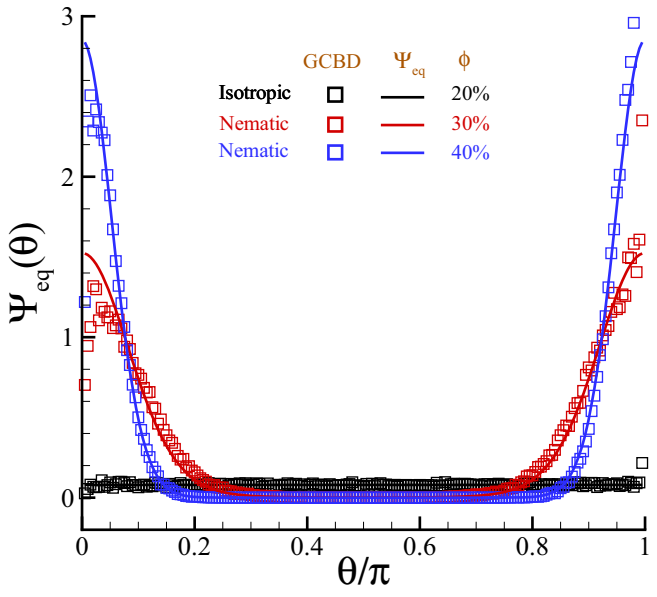

FIG. 5. Examples of orientational PDF for $\gamma = 10$ at $\phi = 20\%,\ 30\%,\ 40\%$. Open squares represent the GCBD data, and the solid lines represent the results by using $\Psi_{\rm eq}$ in Eq. (2).

APPENDIX B: MEASURING D_r FROM QUADRATIC OACFs

Here we construct a mathematical model to connect the quadratic OACF with the Brownian diffusivity D_r defined in Eq. (1). We follow DE's theory [2,28] to define $\langle(\mathbf{p}(t)\cdot\mathbf{p}(0))^2\rangle = \int(\mathbf{pp}{:}\mathbf{p}'\mathbf{p}')G(\mathbf{p},\mathbf{p}';t)\Psi_{\rm eq}(\mathbf{p}')d\mathbf{p}\,d\mathbf{p}'$ where a Green's function $G(\mathbf{p},\mathbf{p}';t)$ represents a conditional (or joint) probability that the probe is in the direction $\mathbf{p}$ at time t, given that it was in the direction $\mathbf{p}(0)$ at $t = 0$. It can be derived from the Smoluchowski equation that the time evolution of $G(\mathbf{p},\mathbf{p}';t)$ follows $\frac{\partial G}{\partial t} = D_r\boldsymbol{\mathcal{R}}\cdot(\boldsymbol{\mathcal{R}}G + \frac{G}{k_BT}\boldsymbol{\mathcal{R}}U_s)$, with the initial condition $G(\mathbf{p},\mathbf{p}';t=0) = \delta(\mathbf{p}-\mathbf{p}')$. Then the time derivative of $\langle(\mathbf{p}(t)\cdot\mathbf{p}(0))^2\rangle$ becomes

$$\begin{aligned}\frac{\partial}{\partial t}\langle[\mathbf{p}(t)\cdot\mathbf{p}(0)]^2\rangle &= D_r\int\left[\boldsymbol{\mathcal{R}}^2(\mathbf{pp}){:}\mathbf{p}'\mathbf{p}' - \frac{1}{k_BT}(\boldsymbol{\mathcal{R}}(\mathbf{pp}){:}\mathbf{p}'\mathbf{p}')\cdot\boldsymbol{\mathcal{R}}U_s\right]\\ &\quad\times G(\mathbf{p},\mathbf{p}';t)\Psi_{\rm eq}(\mathbf{p}')d\mathbf{p}\,d\mathbf{p}'\end{aligned} \tag{B1}$$

with the first term $\boldsymbol{\mathcal{R}}^2(\mathbf{pp}){:}\mathbf{p}'\mathbf{p}' = -6\mathbf{pp}{:}\mathbf{p}'\mathbf{p}' + 2$. Substituting expression of $U_s^{(\rm eq)}$ into the second term, it derives

$$\begin{aligned}-\frac{1}{k_BT}[\boldsymbol{\mathcal{R}}(\mathbf{pp}){:}\mathbf{p}'\mathbf{p}']\cdot\boldsymbol{\mathcal{R}}U_s = \frac{4\zeta_0 S}{k_BT}[(\hat{\mathbf{n}}\hat{\mathbf{n}}\cdot\mathbf{pp}){:}(\mathbf{p}'\mathbf{p}')\\ -(\hat{\mathbf{n}}\cdot\mathbf{p})^2(\mathbf{pp}{:}\mathbf{p}'\mathbf{p}')].\end{aligned} \tag{B2}$$

Then we make an approximation

$$(\hat{\mathbf{n}}\hat{\mathbf{n}}\cdot\mathbf{pp}){:}(\mathbf{p}'\mathbf{p}') = |(\hat{\mathbf{n}}\cdot\mathbf{p}')(\hat{\mathbf{n}}\cdot\mathbf{p})||\mathbf{p}\cdot\mathbf{p}'| \approx (\hat{\mathbf{n}}\cdot\mathbf{p})^2|\mathbf{p}\cdot\mathbf{p}'|. \tag{B3}$$

A Taylor expansion of the above equation yields $|\mathbf{p}\cdot\mathbf{p}'| \approx \frac{1}{2}(\mathbf{pp}{:}\mathbf{p}'\mathbf{p}') + \frac{1}{2}$. The term $(\hat{\mathbf{n}}\cdot\mathbf{p})^2$ can approximated through the steady-state value of $\langle\mathbf{pp}{:}\hat{\mathbf{n}}\hat{\mathbf{n}}\rangle$, which is $(\mathbf{Q}_{\rm eq} + \frac{\mathbf{I}}{3}) : \hat{\mathbf{n}}\hat{\mathbf{n}}$ and it gives $(\hat{\mathbf{n}}\cdot\mathbf{p})^2 \approx \frac{2}{3}S + \frac{1}{3}$. Substituting these into Eq. (B1) and Eq. (B2) gives the evolution over time

$$\begin{aligned}\frac{\partial}{\partial t}\langle[\mathbf{p}(t)\cdot\mathbf{p}(0)]^2\rangle &= -6D_r\left\{(1+q)\langle[\mathbf{p}(t)\cdot\mathbf{p}(0)]^2\rangle - \left(q+\frac{1}{3}\right)\right\}\end{aligned} \tag{B4}$$

with $q(S) = \frac{2\zeta_0}{9k_BT}S(S+\frac{1}{2})$ captures the intrinsic I-N transition. It admits the solution

$$\langle[\mathbf{p}(t)\cdot\mathbf{p}(0)]^2\rangle = \frac{2}{3(1+q)}\exp[-6(1+q)D_rt] + \frac{3q+1}{3(1+q)}. \tag{B5}$$

APPENDIX C: EVALUATING DOUBLE-CONFIGURATIONAL AVERAGES

We perform an analytical calculation of the two configurational averages $\langle|\mathbf{p}\times\mathbf{p}'|\rangle_{p'}^{p}$ and $\langle|\mathbf{p}\cdot\mathbf{p}'|\rangle_{p'}^{p}$. We first define $\mathbf{m}=\mathbf{pp}-\mathbf{I}/3$ and rewrite

$$|\mathbf{p}\cdot\mathbf{p}'|=\sqrt{\mathbf{pp}:\mathbf{p}'\mathbf{p}'}=\sqrt{\frac{1}{3}}\sqrt{1+3\mathbf{m}:\mathbf{m}'},$$
$$|\mathbf{p}\times\mathbf{p}'|=\sqrt{1-\mathbf{pp}:\mathbf{p}'\mathbf{p}'}=\sqrt{\frac{2}{3}}\sqrt{1-\frac{3}{2}\mathbf{m}:\mathbf{m}'}. \quad \text{(C1)}$$

For the first expression in (C1), we perform Taylor expansions in terms of $\mathbf{m}:\mathbf{m}'$, leading to

$$|\mathbf{p}\cdot\mathbf{p}'|=\sqrt{\frac{1}{3}}\left[1+\frac{3}{2}\mathbf{m}:\mathbf{m}'-\frac{9}{8}(\mathbf{m}:\mathbf{m}')^2+\frac{27}{16}(\mathbf{m}:\mathbf{m}')^3+\cdots\right]. \quad \text{(C2)}$$

Then we employ a quadratic closure to express the high-order moments in terms of the lower-order moments, leading to $\langle\overbrace{\mathbf{mm}\cdots\mathbf{mm}}^{N}\rangle_p=\overbrace{\mathbf{QQ}\cdots\mathbf{QQ}}^{N}$. Hence we have

$$\begin{aligned}&\langle|\mathbf{p}\cdot\mathbf{p}'|\rangle_{p'}^{p}\\&\approx\sqrt{\frac{1}{3}}\left[1+\frac{3}{2}\mathbf{Q}:\mathbf{Q}'-\frac{9}{8}(\mathbf{Q}:\mathbf{Q}')^2+\frac{27}{16}(\mathbf{Q}:\mathbf{Q}')^3+\cdots\right]\\&=\sqrt{\frac{1}{3}}\sqrt{1+2S^2}. \quad \text{(C3)}\end{aligned}$$

Similarly, the second term in (C1) can be calculated as

$$\langle|\mathbf{p}\times\mathbf{p}'|\rangle_{p'}^{p}\approx\sqrt{\frac{2}{3}}\sqrt{1-S^2}. \quad \text{(C4)}$$

[1] P. G. DeGennes, *The Physics of Liquid Crystals* (Oxford University Press, Oxford, 1974).

[2] M. Doi and S. Edwards, *The Theory of Polymer Dynamics* (Oxford University Press, New York, 1986).

[3] M. Doi, *Soft Matter Physics* (Oxford University Press, New York, 2013).

[4] S. Woltman, G. Jay, and G. Crawford, Liquid-crystal materials find a new order in biomedical applications, Nat. Mater. **6**, 929 (2007).

[5] T. White and D. Broer, Smectic phase in suspensions of gapped DNA duplexes, Nat. Mater. **14**, 1087 (2015).

[6] M. Salamonczyk, J. Zhang, G. Portale, C. Zhu, E. Kentzinger, J. Gleeson, A. Jakli, C. De Michele, J. Dhont, S. Sprunt, and E. Stiakakis, Smectic phase in suspensions of gapped DNA duplexes, Nat. Commun. **7**, 13358 (2016).

[7] J. P. Hansen and I. R. McDonald, *Theory of Simple Liquids* (Academic Press, New York, 1990).

[8] M. Fixman, Dynamics of Semidilute Polymer Rods: An Alternative to Cages, Phys. Rev. Lett. **55**, 2429 (1985).

[9] G. Vroege and H. Lekkerkerker, Phase transitions in lyotropic colloidal and polymer liquid crystals, Rep. Prog. Phys. **55**, 1241 (1992).

[10] H. Hervet, L. Léger, and F. Rondelez, Self-Diffusion in Polymer Solutions: A Test for Scaling and Reptation, Phys. Rev. Lett. **42**, 1681 (1979).

[11] J. F. Maguire, J. P. McTague, and F. Rondelez, Rotational Diffusion of Sterically Interacting Rodlike Macromolecules, Phys. Rev. Lett. **45**, 1891 (1980).

[12] K. Zero and R. Pecora, Rotational and translational diffusion in semidilute solutions of rigid-rod macromolecules, Macromolecules **15**, 87 (1982).

[13] P. Cobb and J. Butler, Simulations of concentrated suspensions of rigid fibers: Relationship between short-time diffusivities and the long-time rotational diffusion, J. Chem. Phys. **123**, 054908 (2005).

[14] Y. Tao, W. den Otter, J. Padding, J. Dhont, and W. Briels, Brownian dynamics simulations of the self- and collective rotational diffusion coefficients of rigid long thin rods, J. Chem. Phys. **122**, 244903 (2005).

[15] Y. Tao, W. den Otter, J. Dhont, and W. Briels, Isotropic-nematic spinodals of rigid long thin rodlike colloids by event-driven Brownian dynamics simulations, J. Chem. Phys. **124**, 134906 (2006).

[16] A. Raviol, W. Stille, and G. Strobl, The effect of molecular association and tube dilation on the rotational viscosity and rotational diffusion in nematic liquid crystals, J. Chem. Phys. **103**, 3788 (1995).

[17] D. Paparo, L. Marrucci, G. Abbate, E. Santamato, P. Bartolini, and R. Torre, Time resolved fluorescence of dye solutions in nematic liquid crystals, Mol. Crystals Liquid Crystals Sci. Tech. A **282**, 461 (1996).

[18] J. Jadżyn and G. Czechowski, Interactions and dynamics of mesogenic molecules in the vicinity of the isotropic to nematic phase transition, J. Mol. Struct. **844**, 59 (2007).

[19] A. Perera and G. N. Patey, The solution of the hypernetted-chain and Percus–Yevick approximations for fluids of hard spherocylinders, J. Chem. Phys. **89**, 5861 (1988).

[20] H. Graf and H. Löwen, Density functional theory for hard spherocylinders: Phase transitions in the bulk and in the presence of external fields, J. Phys.: Condens. Matter **11**, 1435 (1999).

[21] W. Yan, H. Zhang, and M. Shelley, Computing collision stress in assemblies of active spherocylinders: Applications of a fast and generic geometric method, J. Chem. Phys. **150**, 064109 (2019).

[22] P. Bolhuis, A. Stroobants, D. Frenkel, and H. Lekkerkerker, Numerical study of the phase behavior of rodlike colloids with attractive interactions, J. Chem. Phys. **107**, 1551 (1997).

[23] W. Maier and A. Saupe, Eine einfache molekulare Theorie des nematischen kristallinflüssigen Zustandes, Zeit. Nat. Teil A **13**, 564 (1958).

[24] B. Ezhilan, M. Shelley, and D. Saintillan, Instabilities and nonlinear dynamics of concentrated active suspensions, Phys. Fluids **25**, 070607 (2013).

[25] T. Gao, R. Blackwell, M. A. Glaser, M. D. Betterton, and M. J. Shelley, Multiscale Polar Theory of Microtubule and Motor-Protein Assemblies, Phys. Rev. Lett. **114**, 048101 (2015).

[26] W. Yan and J. F. Brady, Anisotropic swim stress in active matter with nematic order, New J. Phys. **20**, 053056 (2018).

[27] A. Perera, S. Ravichandran, M. Moreau, and B. Bagchi, Single particle and collective orientational relaxation in an anisotropic liquid near the isotropic-nematic transition, J. Chem. Phys. **106**, 1280 (1997).

[28] B. Berne and R. Pecora, *Dynamic Light Scattering* (Wiley, New York, 1976).

[29] I. Dozov, S. Temkin, and N. Kirov, Two-stage model for molecular orientational relaxation in liquid crystals, Liquid Crystals **8**, 727 (1990).

[30] J. Jadzyn, L. Hellemans, G. Czechowski, C. Legrand, and R. Douali, Dielectric and viscous properties of 6CHBT in the isotropic and nematic phases, Liquid Crystals **27**, 613 (2000).

[31] J. Jadżyn, G. Czechowski, J.-L. Dejardin, and M. Ginovska, Anomalous rotational diffusion in the vicinity of the isotropic to nematic phase transition, J. Phys.: Condens. Matter **17**, 813 (2005).

[32] H. Löwen, Brownian dynamics of hard spherocylinders, Phys. Rev. E **50**, 1232 (1994).

[33] D. Saintillan and M. Shelley, Orientational Order and Instabilities in Suspensions of Self-Locomoting Rods, Phys. Rev. Lett. **99**, 058102 (2007).

[34] S. Peroukidis, K. Lichtner, and S. H. L. Klapp, Tunable structures of mixtures of magnetic particles in liquid-crystalline matrices, Soft Matter **11**, 5999 (2015).

[35] D. Frenkel and J. Maguire, Molecular dynamics study of the dynamical properties of an assembly of infinitely thin hard rods, Mol. Phys. **49**, 503 (1983).

[36] J. Rallison, Brownian diffusion in concentrated suspensions of interacting particles, J. Fluid Mech. **186**, 471 (1988).

[37] M. Doi, Molecular dynamics and rheological properties of concentrated solutions of rodlike polymers in isotropic and liquid crystalline phases, J. Polym. Sci. Polym. Phys. Ed. **19**, 229 (1981).

[38] J. Feng, C. Chaubal, and L. Leal, Closure approximations for the Doi theory: Which to use in simulating complex flows of liquid-crystalline polymers, J. Rheol. **42**, 1095 (1998).